Available online at www.sciencedirect.com
ScienceDirect
Journal of Sound and Vibration 324 (2009) 283–296
JOURNAL OF SOUND AND VIBRATION
www.elsevier.com/locate/jsvi

Introduction of damping into the flexible multibody belt-drive model: A numerical and experimental investigation

Gregor Čepon[a], Lionel Manin[b], Miha Boltežar[a,*]

[a]University of Ljubljana, Faculty of Mechanical Engineering, Aškerčeva 6, 1000 Ljubljana, Slovenia
[b]Université de Lyon, CNRS, INSA de Lyon, LaMCoS UMR 5259, Villeurbanne F-69621, France

Received 11 July 2008; received in revised form 28 January 2009; accepted 2 February 2009
Handling Editor: M.P. Cartmell
Available online 5 March 2009

Abstract

In this paper the belt-drive model using an absolute nodal coordinate formulation is presented. Using this approach the damping forces are usually neglected and only the elastic forces are taken into account. The aim of this paper is to introduce a damping mechanism into the belt-drive model and to verify it against experimental data. Different damping mechanisms are proposed for the damping of the longitudinal and bending deformations and several experiments were conducted in order to obtain the damping properties. Good agreement between the numerical result and the experimentally obtained data was found. Finally, the applicability of the belt-drive model was presented in a comparison with the pinned–pinned beam model.

1. Introduction

Belt drives are commonly used to transmit power in many engineering applications, such as automotive engines, industrial machines, etc. Due to their simple installation and low maintenance, together with an ability to absorb shocks, they are frequently used instead of chain or geared transmission systems. However, they can exhibit complex dynamic behaviors, such as the transverse vibrations of the belt spans, tension fluctuations, sliding of the belt over the pulley, etc. All this phenomena impact the belt life and also the acoustic comfort. It is, therefore, very important to find an effective and validated approach for predicting the dynamic response of such belt drives. The literature regarding belt drives is extensive; in Ref. [1] a thorough literature review up to 1992 can be found. In addition, there are numerous studies dealing with rotational responses [2–5], the transverse vibrations of belt spans [6–8,26], etc.

Leamy and Wasfy [9,10] proposed a general, dynamic finite-element model, where the belt is modelled using truss elements. The finite-element model is able to predict the belt creep over the pulley and the belt-drive vibrations. Using the absolute nodal coordinate formulation (ANCF), originally proposed by Shabana [11], the authors in Ref. [12] developed a more general planar model of a belt drive. The belt was modelled using a

*Corresponding author. Tel.: +386 1 4771 608; fax: +386 1 2518 567.
E-mail address: miha.boltezar@fs.uni-lj.si (M. Boltežar).

0022-460X/$ - see front matter © 2008 Elsevier Ltd. All rights reserved.
doi:10.1016/j.jsv.2009.02.001

two-dimensional shear deformable beam element that accounts for both the bending and longitudinal stiffness. An extended formulation for three-dimensional belt drives was presented in Ref. [13]. Most recently, Čepon and Boltežar [14] presented a belt-drive model using ANCF with detailed contact formulation between belt and pulley. The belt–pulley contact was formulated as linear complementarity problem (LCP), using the discontinuous Coulomb friction law to model frictional forces.

The researchers, using the ANCF for the belt-drive modelling, usually did not account for any dissipative mechanism except in Ref. [14] where the damping mechanism for longitudinal deformations is proposed. Belt materials such as plastic, metal or ceramic-reinforced composite materials and polymer materials do not obey Hooke's law, but usually exhibit viscoelastic behavior [15]. The ANCF is quite recent, so it has generated little literature on damping [16]. Takahashi et al. [17] introduced a Rayleigh proportional damping matrix to a beam model, assuming that the longitudinal deformations within each flexible body are small. The proportional damping matrix is obtained as a linear combination of a constant-mass and constant-bending stiffness matrix. This model was also used in Refs. [18,19], where the results were also checked against experimental data. With this damping model the rigid-body motions are also damped. However, the damping of longitudinal deformations cannot be formulated in this way due to the nonlinear structure of the longitudinal stiffness matrix, even when small deformations are considered. The internal damping force model, for the ANCF, based on the continuum mechanics approach, is presented in Ref. [16]. This model dissipates the energy only when the system experiences some deformations, whereas the rigid-body motions are not damped.

In this paper we have used the ANCF to model belt drives with a poly-V belt. Additionally, we have included a damping mechanism into the formulation. The damping mechanism is a combination of proportional and internal damping models. For the damping of the bending deformations, Rayleigh proportional damping is proposed, as presented in Ref. [17]. For longitudinal deformations the internal damping mechanism adopting viscoelastic material is proposed. To identify the damping characteristics and other belt-material properties, several experiments were performed. The damping mechanism is additionally included into the belt-drive model and a comparison between the simulations and the experiments is also made in order to validate the proposed belt-drive model. Although in this study a non-operating two-pulley belt drive is proposed for identifying the belt-material properties, the presented belt-drive model is general. With the proposed contact formulation between the belt and the pulley it is possible to simulate belt drives with several pulleys, and even tensioner pulleys in arbitrary operational conditions, see Ref. [14].

This paper is organized as follows. In Section 2 the model of the belt drive with the formulation of the damping forces is presented. Section 3 presents the contact formulation between the belt and the pulley. In Section 4 the identification of the damping and the other belt-material properties are presented. Next, a comparison between the simulations and the experiments is given. Finally, in Section 5, the conclusions are drawn.

2. Formulation of belt-drive model using the ANCF

The belt is modelled as a system of planar beam elements, using flexible multibody dynamics. An ANCF is proposed, which can be used in a large rotation and deformation analysis of flexible bodies that undergo arbitrary displacements. The two-dimensional beam element is based on the element originally proposed by Berzeri and Shabana [20]. In contrast to the study presented in Ref. [12], this element does not include a shear deformation. However, here we have additionally included a dissipative mechanism in the belt model. The presented damping model is a combination of an internal damping model and Rayleigh proportional damping. The internal damping-force model is based on the continuum mechanics approach, as presented in Ref. [16] for three-dimensional beams and plates. As is the case in this study, the two-dimensional beam element is adopted for the belt model, but the formulation of the damping matrix is simpler. For this reason the derivation of the elastic and damping forces is presented in more detail. A viscoelastic belt material that obeys the Kelvin–Voigt model is described by the following constitution relation [15]:

$$\sigma_l(x,t) = E\varepsilon_l(x,t) + c\frac{\partial \varepsilon_l(x,t)}{\partial t}, \tag{1}$$

where σ_l is the longitudinal distributed stress, E is Young's modulus, c is the viscoelastic damping factor and ε_l is the Lagrangian strain:

$$\varepsilon_l = \frac{1}{2}(\mathbf{r}'^{\mathrm{T}}\mathbf{r}' - 1), \quad \mathbf{r}' = \frac{\mathrm{d}\mathbf{r}}{\mathrm{d}x}, \quad \mathbf{r} = \mathbf{S}(x)\mathbf{e}^j. \tag{2}$$

The vector $\mathbf{r}$ defines the coordinates of an arbitrary point on the beam axis, the matrix $\mathbf{S}(x)$ is the global shape function, and $\mathbf{e}^j$ is the vector of the element nodal coordinates belonging to the element j. The virtual work due to the elastic and dissipative forces can be written as follows:

$$\delta W_l = \int_V \sigma_l \delta\varepsilon_l \,\mathrm{d}V, \tag{3}$$

where $\delta\varepsilon_l$ is the virtual change of the longitudinal strain and V is the volume. Assuming that the cross-section A is constant and the material is isotropic, the virtual work due to the longitudinal deformation is given as

$$\delta W_l = EA\mathbf{e}^{j^{\mathrm{T}}} \int_0^L \varepsilon_l \mathbf{S}_L \,\mathrm{d}x \delta\mathbf{e}^j + cA\mathbf{e}^{j^{\mathrm{T}}} \int_0^L \frac{\partial\varepsilon_l}{\partial t}\mathbf{S}_L \,\mathrm{d}x \delta\mathbf{e}^j, \tag{4}$$

where

$$\varepsilon_l = \frac{1}{2}(\mathbf{e}^{j^{\mathrm{T}}}\mathbf{S}_L\mathbf{e}^j - 1), \quad \delta\varepsilon_l = \frac{\partial\varepsilon_l}{\partial\mathbf{e}^j}\delta\mathbf{e}^j = \mathbf{e}^{j^{\mathrm{T}}}\mathbf{S}_L\delta\mathbf{e}^j, \quad \mathbf{S}_L = \mathbf{S}'^{\mathrm{T}}\mathbf{S}'. \tag{5}$$

Here, $\delta\mathbf{e}^j$ is the virtual change of the element's generalized coordinates and L is the length of the belt element. The vector of generalized forces due to the longitudinal deformation associated with the element j can be written as [14]

$$\mathbf{Q}_l^j = (\mathbf{K}_l^j + \mathbf{C}_l^j)\mathbf{e}^j, \quad \mathbf{K}_l^j = EA\int_0^L \varepsilon_l \mathbf{S}_L \,\mathrm{d}x, \quad \mathbf{C}_l^j = cA\int_0^L \frac{\partial\varepsilon_l}{\partial t}\mathbf{S}_L \,\mathrm{d}x, \tag{6}$$

where $\mathbf{K}_l^j$ and $\mathbf{C}_l^j$ are the nonlinear longitudinal stiffness and damping matrices. The virtual work accounting for the bending moment can be rewritten as

$$\delta W_M = \int_0^L M\delta\kappa \,\mathrm{d}x, \tag{7}$$

where I is the moment of inertia of the beam's cross-section, κ is the curvature of the beam and M is the bending moment:

$$M = EI\kappa + cI\frac{\partial\kappa}{\partial t}. \tag{8}$$

Assuming small, longitudinal deformations, the curvature of the beam can be simplified as follows:

$$\kappa \simeq \left|\frac{\mathrm{d}^2\mathbf{r}}{\mathrm{d}x^2}\right|. \tag{9}$$

Taking into account only the elastic forces and using Eq. (9) the vector of the generalized bending forces takes the simple form

$$\mathbf{Q}_M^j = \mathbf{K}_M^j\mathbf{e}^j, \qquad \mathbf{K}_M^j = EI\int_0^L \mathbf{S}''^{\mathrm{T}}\mathbf{S}'' \,\mathrm{d}x, \tag{10}$$

where $\mathbf{K}_M^j$ is the constant-bending stiffness matrix. The derivation of the bending damping matrix from Eq. (7) is tedious and the expressions in the resulting matrix are long and highly nonlinear. This results in longer computation times, which lead to a significantly increased computation time for the entire simulation. In order to avoid the computing of the nonlinear bending matrix, Rayleigh proportional damping is used to formulate the damping of the bending deformations. The constant-mass matrix $\mathbf{M}_B^j$ and the constant-bending stiffness matrix $\mathbf{K}_M^j$ are used to formulate the constant Rayleigh damping matrix for the bending deformation as [17]

$$\mathbf{C}^j = \alpha\mathbf{M}_B^j + \beta\mathbf{K}_M^j. \tag{11}$$

The computation of Rayleigh's parameters α and β is explained in Section 4.2.3. With this procedure the rigid-body motions in the element are also damped. However, it can be demonstrated that Rayleigh proportional damping has an influence mainly on the damping of the bending deformations and a small influence on the damping of longitudinal deformations. Finally, we can see that for the damping of longitudinal deformations the internal damping model is used, and for the damping of bending deformations, Rayleigh proportional damping is applied. Two different damping mechanisms for longitudinal and bending deformations in the belt model are actually justified, because the belt is a composite and the damping properties in the longitudinal and transverse directions may differ.

Taking into account the presented damping mechanisms, the equation of motion for the belt segment j can be written as

$$\mathbf{M}_B^j\ddot{\mathbf{e}}^j + \underbrace{(\alpha\mathbf{M}_B^j + \beta\mathbf{K}_M^j)\dot{\mathbf{e}}^j + (\mathbf{K}_l^j + \mathbf{C}_l^j + \mathbf{K}_M^j)\mathbf{e}^j}_{-\mathbf{Q}_f^j} = \mathbf{Q}_{eB}^j. \tag{12}$$

The system of the equations of motion, including all the beam elements in the belt and the constraint equations describing the connectivity constraints, can be written as

$$\begin{bmatrix} \mathbf{M}_B & \mathbf{C}_{eB}^{\mathrm{T}} \\ \mathbf{C}_{eB} & \mathbf{0} \end{bmatrix} \begin{Bmatrix} \ddot{\mathbf{e}} \\ \boldsymbol{\lambda}_B \end{Bmatrix} = \begin{bmatrix} \mathbf{Q}_f + \mathbf{Q}_{eB} \\ \mathbf{Q}_{dB} \end{bmatrix}, \tag{13}$$

where $\mathbf{M}_B$ is the constant-mass matrix of the belt [11], $\mathbf{C}_{\mathbf{e}B}$ is the Jacobian of the constraint equations, $\boldsymbol{\lambda}_B$ is the vector of the Lagrange multipliers. The vector $\mathbf{Q}_{eB}$ is the generalized force vector that includes external forces, $\mathbf{Q}_f$ is the generalized force due to the stiffness and damping forces and the vector $\mathbf{e} = \{\mathbf{e}^1, \ldots, \mathbf{e}^{n_B}\}^{\mathrm{T}}$ includes the generalized coordinates of all the belt elements. Vector $\mathbf{Q}_{dB}$ is obtained through differentiation of the constraints:

$$\mathbf{Q}_{dB} = -\frac{\partial(C_{\mathbf{e}B}\dot{\mathbf{e}})}{\partial\mathbf{e}}\dot{\mathbf{e}}. \tag{14}$$

The pulley is modelled as a rigid cylinder, and it is connected to the ground by the revolute joint. The equations of motion for all the pulleys in the system can be written in a similar form as Eq. (13). All the equations of motion for the belt and the pulleys are then put together and solved simultaneously, taking into consideration the contact forces between the belt and the pulley.

3. Contact formulation between the belt and the pulley

In a belt drive, the belt is constrained to move over the surface of the pulley. Although the aim of this study is to identify the belt-material properties on a non-operating belt drive, the presented contact model is also valid for operational belt drives. Both the normal reaction force F_N and the tangential friction force F_T are generated when the belt element contacts the pulley's surface. In this study we have adopted the belt–pulley contact formulation as presented in Ref. [14].

Each belt element has five possible contact points, which are equally spaced along the length of the element. The normal reaction forces of each contact point are computed using the penalty method:

$$F_N^i = K_P g_N^i + C_P \dot{g}_N^i, \tag{15}$$

where g_N^i is the penetration of the contact point i on the belt segment into the pulley. Similarly, $\dot{g}_N^i$ denotes the penetration velocity of the contact point i in the normal direction, see Fig. 1, and K_P and C_P are penalty parameters. In the tangential contact direction we use the representation of Coulomb's friction law on the acceleration level:

$$\left.\begin{array}{lll} \text{sticking:} & |F_T^i| < \mu_0 F_N^i & \Longrightarrow \quad |\ddot{g}_T^i| = 0, \\ \text{sliding:} & |F_T^i| = \mu_0 F_N^i & \Longrightarrow \quad |\ddot{g}_T^i| > 0, \end{array}\right\} \quad i \in I_H, \tag{16}$$

where μ_0 is the coefficient of friction, the set I_H contains all possible sticking contacts and $\ddot{g}_T^i$ is the relative acceleration in tangential direction. In order to compute the possible sticking forces the contact problem in the

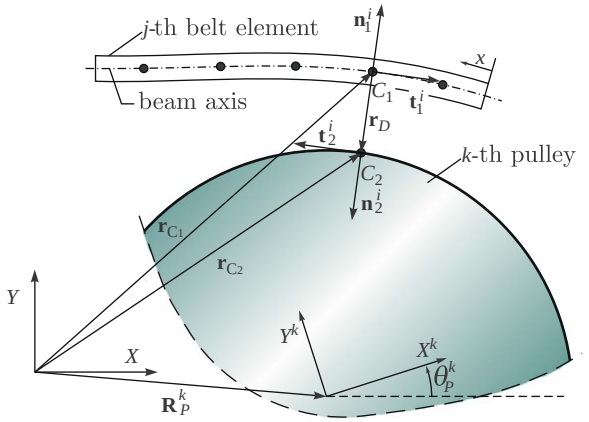

Fig. 1. Belt–pulley contact formulation.

tangential direction has to be formulated as an LCP. To formulate the LCP in the tangential direction the proposed method in Ref. [21] can be applied. The resulting LCP is in the following standard form:

$$\mathbf{y} = \mathbf{A}\mathbf{x} + \mathbf{b}, \quad \mathbf{y} \geqslant \mathbf{0}, \quad \mathbf{x} \geqslant 0, \quad \mathbf{y}^{\mathrm{T}}\mathbf{x} = \mathbf{0}, \tag{17}$$

and it can be solved using, for example, the Lemke algorithm [22]. From the computed contact forces the generalized accelerations of the belt-drive system can be determined. Finally, generalized coordinates can be obtained from an integration, using, for example, the fourth-order Runge–Kutta integration scheme.

4. Investigation on the belt-material properties

In this section the methods for identifying the damping and stiffness properties of the belt material are presented. A poly-V belt (5pk1200) was examined by using two different experimental setups in order to obtain the material properties in the longitudinal and transverse directions. The friction coefficient between belt and pulley is $\mu_0 = 1.2$. Two different experimental setups were considered in order to obtain the material properties in the longitudinal and transverse directions. In both cases the free and forced responses were investigated.

4.1. Longitudinal direction

In order to determine experimentally the belt-material properties in the longitudinal direction the method presented in Ref. [23] is proposed. The belt is suspended to the rigid frame at one end and, at the other end, to the mass, as shown in Fig. 2(a). The system can be idealized as a weight attached to a spring and a damper mounted in parallel, see Fig. 2(b). The longitudinal excitation of the belt is made with a shock hammer. From the damped free response of the system the resonant frequency and the damping ratio can be determined. First, the experimentally obtained natural frequencies and the corresponding damping ratio can help determine the belt's longitudinal stiffness EA and the viscoelastic damping property cA using the following equations:

$$EA = \omega_0^2 mL, \quad cA = 2\delta mL\omega_0, \tag{18}$$

where m is the mass of the weight, L is the length of the belt segment, ω_0 is the measured natural frequency and δ is the measured damping ratio. Damping in the longitudinal direction is also affected by the Rayleigh damping model as it also damps rigid-body motions. However, it can be demonstrated that for the values of α and β that are typical for the investigated poly-V belt, the damping of the longitudinal deformations is negligible.

In Table 1 the measured natural frequencies and damping ratios for different lengths of belt segment are presented. The computed belt-material properties in the longitudinal direction are determined per individual

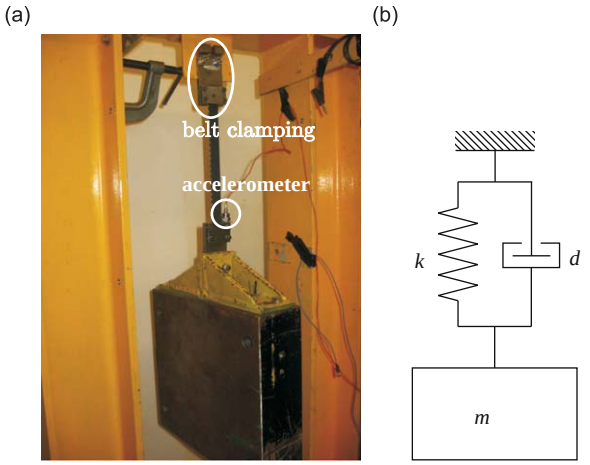

Fig. 2. Longitudinal damping and stiffness measurement: (a) experimental setup; (b) analytical model.

Table 1
Measured modal parameters in the longitudinal direction.

L (m)	m (kg)	f_0 (Hz)	δ	EA (N/rib)	cA (N s/rib)
0.2	66.4	16.9	0.007	3×10^4	4
0.3	66.4	13.7	0.0065	2.9×10^4	4.5
0.39	66.4	12.5	0.005	3.2×10^4	3.8
Average				3×10^4	4.1

rib. The stiffness and the damping characteristics differ with the length of the belt specimen and with the mass of the weight. However, the influence of the weight mass on the stiffness and damping properties is considerably smaller than the influence of the belt specimen length. This was already reported in Ref. [24] and is mainly the effect of the belt clamping at the ends.

In order to verify the flexible, multibody belt model in the longitudinal direction, the experimental setup presented in Fig. 3(a) is proposed. The weight that is clamped to the belt is excited with the shaker. The conventional frequency–response function (FRF) estimator $H_1(\omega)$ is used:

$$H_1(\omega) = \frac{S_{fx}(\omega)}{S_{ff}(\omega)}, \tag{19}$$

where $S_{fx}(\omega)$ is the cross-input–output spectrum and $S_{ff}(\omega)$ is the input auto-spectrum. The simulated FRF is compared with the experimentally obtained FRF. The simulated FRF is obtained using the flexible multibody model presented in Fig. 3(b). Because the ANCF results in nonlinear system of equations the FRF has to be computed explicitly using direct numerical integration. It can be seen from the measured data that the response of the belt-weight system is linear. This implies that the flexible multibody model of the experimental setup should give a linear response. From the simulated displacement response of the weight and the applied force we can compute the FRF using Eq. (19).

In Fig. 4 the measured and simulated FRFs are presented for different lengths of the belt segment. The good agreement between the measured and simulated FRFs prove that material properties obtained using one-degree-of-freedom model can be used in the nonlinear ANCF approach for modelling of the belt drives.

4.2. Transverse direction

In the transverse direction the displacement response is mainly governed by the bending deformations. In this section we will present the identification of the bending rigidity modulus EI and the damping parameters

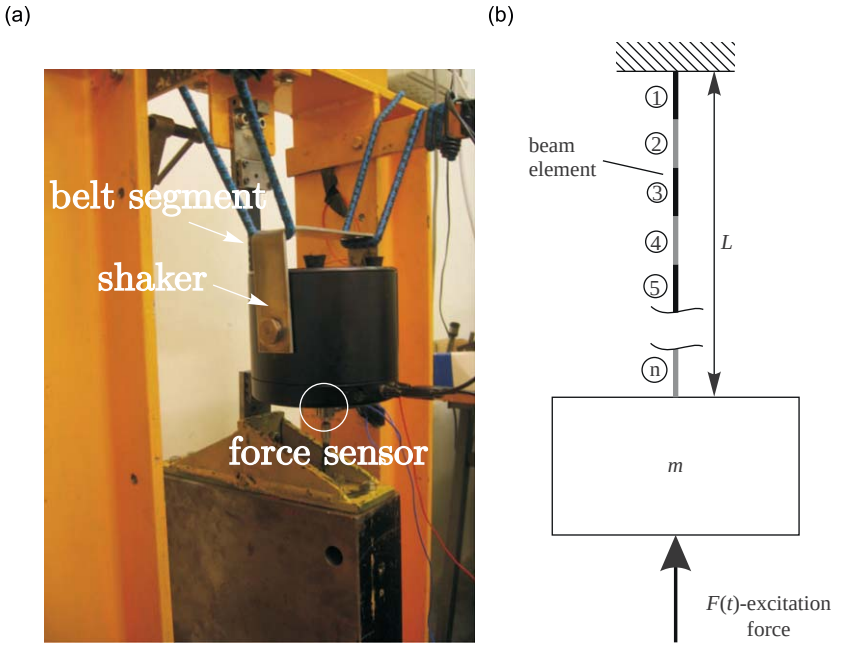

Fig. 3. Forced response of the belt-weight system: (a) experimental setup; (b) numerical model.

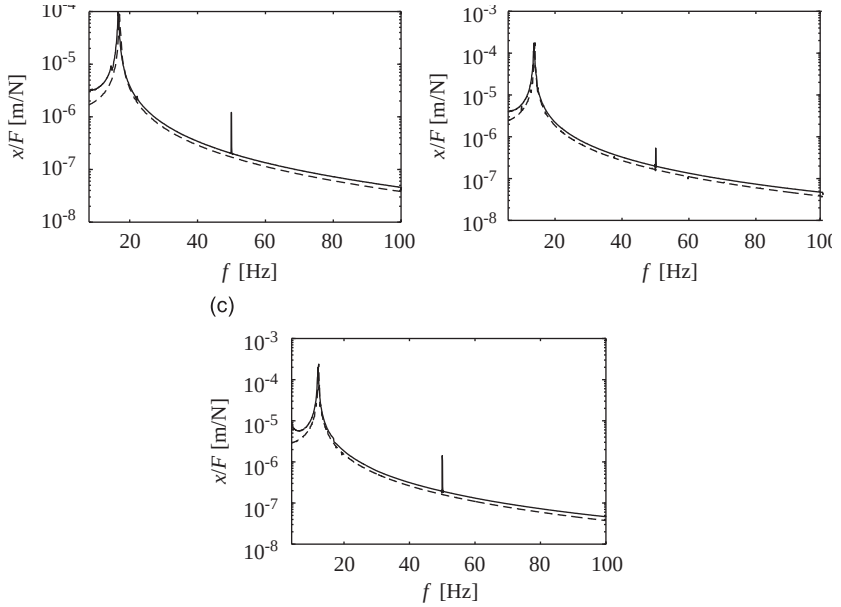

Fig. 4. FRF of the belt-weight system in the longitudinal direction: (a) $L = 0.2$ m; (b) $L = 0.3$ m; (c) $L = 0.39$ m. (——) experiment, (– – –) numerical simulation.

α and β using a two-pulley belt-drive experimental setup. The simulated results are compared with experimentally obtained data.

4.2.1. Identification of the bending rigidity modulus

The bending rigidity modulus EI of the belt can be determined from the free response of the belt span in the transverse direction. The non-operating two-pulley belt drive is considered as shown in Fig. 5(a).

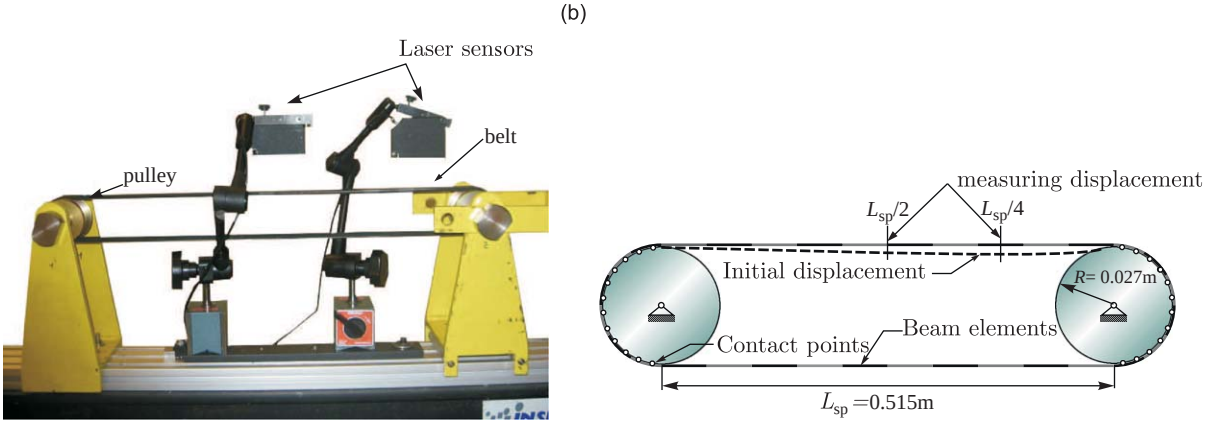

Fig. 5. Bending rigidity modulus identification: (a) experimental setup; (b) numerical model.

The transverse displacement of the belt span is measured with two laser sensors positioned at the middle and the quarter length of the belt span. Assuming that the damping is low the natural frequencies can be obtained from the free response of the belt span. The ith measured natural frequency $f_{0i}^{\exp}$ can then be compared with the calculated natural frequencies f_{0i} of a pre-tensioned pinned–pinned beam [1]:

$$f_{0i} = \sqrt{\frac{EI}{\rho}\left(\frac{\pi i^2}{2L_{sp}^2}\right)^2 + \frac{F}{\rho}\left(\frac{i}{2L_{sp}}\right)^2}, \tag{20}$$

where i is the mode shape and ρ is the mass per unit length of the belt. The computation of the bending rigidity modulus EI can be determined as a result of the optimization process in the least-squares sense:

$$\min_{EI} \frac{1}{2}\sum_k \left| \begin{pmatrix} f_{01}(EI,F_k) - f_{01}^{\exp}(EI,F_k) \\ f_{02}(EI,F_k) - f_{02}^{\exp}(EI,F_k) \\ f_{03}(EI,F_k) - f_{03}^{\exp}(EI,F_k) \end{pmatrix} \right|^2, \tag{21}$$

where F_k is the belt's longitudinal force. Using Eq. (21) the optimized value is $EI = 9.6 \times 10^{-3}\,\mathrm{N\,m^2/rib}$.

In the experimental setup, the belt is wrapped around the pulley, which certainly has an influence on the natural frequencies of the belt span. Hence, the proposed two-pulley belt-drive model (Fig. 5(b)) is used with the ANCF and the belt is modelled using 32 beam elements. Because the finite-element formulation is nonlinear the natural frequencies of the upper span cannot be obtained using implicit methods, but instead have to be obtained explicitly using numerical integration. Numerical integration was preformed using variable order Adams–Bashforth–Moulton method. To simulate the free response, the upper belt span is initially displaced and then released from rest. Using this method the resulting optimized bending rigidity modulus is $EI = 5.2 \times 10^{-3}\,\mathrm{N\,m^2/rib}$, and it is smaller than the one obtained using the analytical equation (20). Wrapping the belt around the pulley increases the belt span's natural frequency, which results in a lower computed bending rigidity modulus. Because the advanced, flexible, multibody model of the two-pulley belt drive is more realistic, the bending rigidity modulus obtained by this method is more accurate. In Table 2 the experimentally obtained natural frequencies are compared to the frequencies obtained using the analytical equation and using the advanced, flexible, multibody model.

4.2.2. *Measurement of the damping ratio*

For an alone belt span, the damping in the transverse direction is mainly governed by the damping of the bending deformations. To identify the two parameters α and β of Rayleigh proportional damping the experimental setup presented in Fig. 6 is proposed. The belt span is excited with the shaker at the left-hand end of the belt span. The applied force is then measured with a force sensor and the transverse displacement with laser sensors positioned at $L_{sp}/4$ and $L_{sp}/6$ from the right end. The belt is subjected to a random excitation

Table 2
First three measured natural frequencies of the belt span in comparison with the numerical models.

F (N)	Experimental natural-frequencies (Hz)			Analytical model (Hz)			Flexible multibody model (Hz)		
	f_1^{exp}	f_2^{exp}	f_3^{exp}	$EI = 9.6 \times 10^{-3}$ N m^2/rib			$EI = 5.2 \times 10^{-3}$ N m^2/rib		
				f_1	f_2	f_3	f_1	f_2	f_3
198	45.3	90.5	135.7	44.3	89.7	137.4	44.9	89.8	138.6
297	54.5	109.3	163.8	53.2	107.4	163.5	54.6	109.3	164
396	62.5	125.4	188.1	61.4	123.7	187.6	62.5	125	187.5
495	69	138.3	207.3	68.6	138	209	70.3	138.6	208.9
594	76.1	153.4	228.4	75.1	151	228.2	76.1	152.3	228.5
693	82.1	164.3	246.5	81.2	163	246	82	164	248

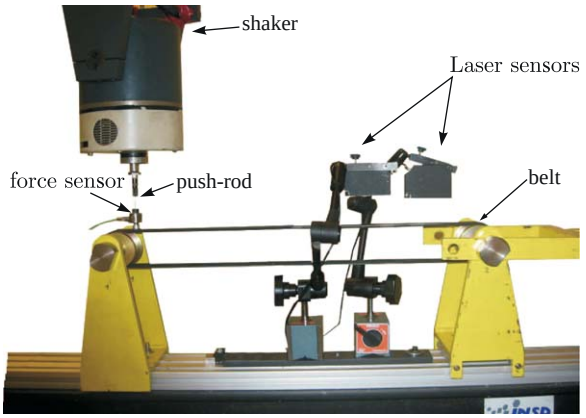

Fig. 6. Experimental setup for damping identification in the transverse direction.

force. The experimental FRFs versus the belt's longitudinal force, obtained using Eq. (19), are presented in Fig. 7. The first three natural frequencies are the most representative, thus the corresponding damping ratios will be used for the damping identification.

The damping ratios are identified using the circle-fitting method, as presented in Ref. [25]. By representing the FRF on a Nyquist diagram we obtain an approximate circle around each natural frequency. The computation of the modal parameters relies on the fitting of the circle to the frequency–response curve near the natural frequency. When using this method the damping model is assumed to be hysteretic and the damping factor is obtained using the following equation:

$$\eta_r = \frac{f_a^2 - f_b^2}{f_r^2} \frac{1}{\tan(\Delta\theta_a) + \tan(\Delta\theta_b)}, \tag{22}$$

where η_r is the hysteretic damping loss factor and f_r the natural frequency associated with the mode r. The f_a represents the frequencies above natural frequency and f_b represents the frequencies below natural frequency. In our case the damping model is viscous. For low damping the hysteretic damping ratio and the viscous damping ratio are approximately related by $2\xi = \eta$.

In Fig. 8(a) the Nyquist diagram around the second natural frequency is presented at the location $L_{sp}/4$ and the belt longitudinal force 495 N. It is possible to derive several values for η_r, depending on the pair of data points that are used in Eq. (22). The results for η_r that depend on the frequencies f_a and f_b can be represented as shown in Fig. 8(b). The best results are obtained when the angles $\Delta\theta_a$ and $\Delta\theta_b$ are not very small and have

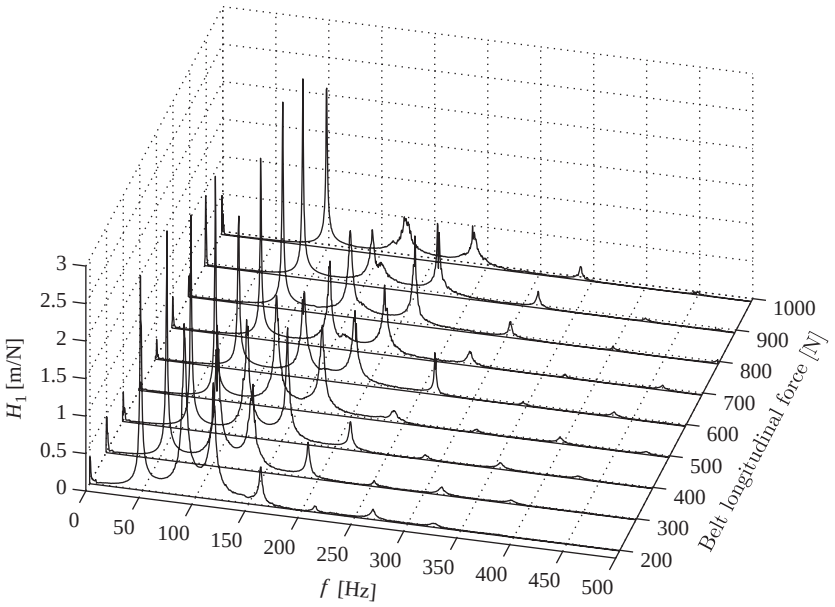

Fig. 7. Measured FRF at position $L_{sp}/4$ versus the belt's longitudinal force.

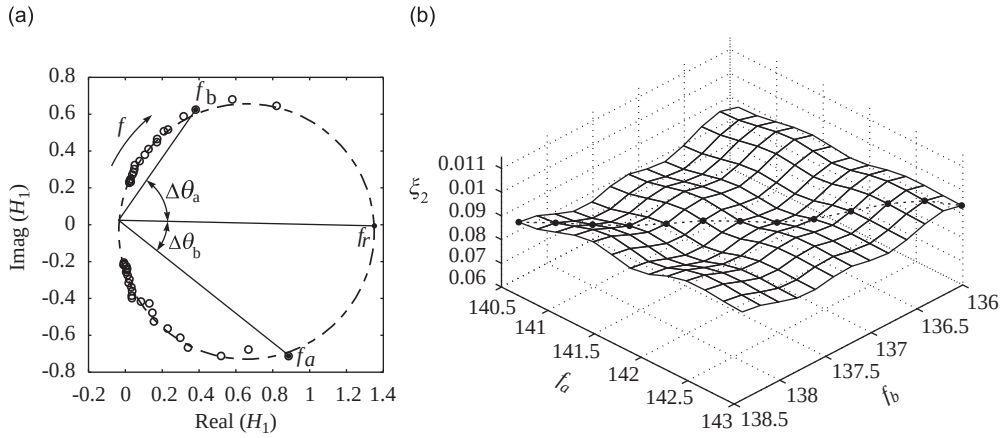

Fig. 8. Determination of ξ_2 using several combinations of data points at location $L_{sp}/4$ and belt longitudinal force 495 N: (a) circle-fit approach; (b) ξ_2 surface.

similar values. Thus, the mean value can be obtained as a combination of the data points corresponding to the diagonal of the ξ surface represented in Fig. 8(b).

Using the above-mentioned method the damping ratios computed at positions $L_{sp}/4$ and $L_{sp}/6$ are presented in Table 3. It was observed that measuring the damping ratio at different locations on the belt's span has practically no influence.

4.2.3. Identification of the Rayleigh parameters

The Rayleigh parameters α and β are identified using the previously measured damping ratios. Because the finite-element formulation results in a nonlinear longitudinal stiffness matrix the orthogonal properties cannot be used for the computation of the parameters α and β. In order to identify these two parameters, an optimization procedure is proposed. The simulated response is obtained using the belt-drive model presented

Table 3
Measured damping ratios corresponding to the first three modes.

F (N)	Damping ratio at $L_{sp}/4$			Damping ratio at $L_{sp}/6$		
	ξ_1	ξ_2	ξ_3	ξ_1	ξ_2	ξ_3
198	0.007	0.017	0.017	0.006	0.016	0.016
297	0.005	0.014	0.015	0.006	0.014	0.014
396	0.004	0.013	0.008	0.005	0.012	0.008
495	0.004	0.010	0.008	0.004	0.010	0.008
594	0.005	0.010	0.007	0.005	0.010	0.008
693	0.003	0.008	0.008	0.004	0.009	0.008

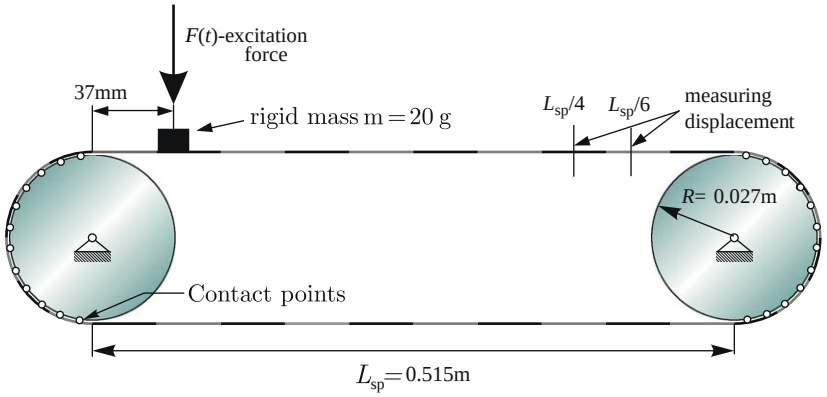

Fig. 9. Flexible multibody model for the identification of the damping parameters.

in Fig. 9. The belt is excited with a random force applied at the same position as in the experimental setup. The mass of the mounting plate and the transducer base is approximately 20 g, and it is not negligible compared to the belt-span mass of 49 g. Therefore, it has to be accounted for in the belt-drive model as a rigid body attached to the belt.

From the simulated displacement response and the known excitation force we can obtain the FRF using Eq. (19). From the FRF the damping ratio can be estimated and the damping parameters α and β can be obtained using the following optimization process:

$$\min_{\alpha,\beta} \frac{1}{2} \sum_{k} \left| \begin{pmatrix} \xi_1(\alpha,\beta,F_k) - \xi_1^{\exp}(F_k) \\ \xi_2(\alpha,\beta,F_k) - \xi_2^{\exp}(F_k) \\ \xi_3(\alpha,\beta,F_k) - \xi_3^{\exp}(F_k) \end{pmatrix} \right|^2, \tag{23}$$

where ξ_i is the damping ratio obtained from the simulated FRF corresponding to the mode i. Similarly, $\xi_i^{\exp}$ is the damping ratio obtained from the experimental FRF corresponding to the mode i. The computed, optimized damping parameters are, in our case, equal to $\alpha = 2.8/\mathrm{s}$ and $\beta = 1.8 \times 10^{-4}\,\mathrm{s}$.

4.2.4. Comparison of the simulations and the experiments

The optimized material properties of Table 4 are used to obtain the predicted damping ratio values which are then compared to the measured ones, see Fig. 10. The damping ratios corresponding to the first and third modes are in good agreement. However, some difference appears for the second mode damping ratios especially at low longitudinal forces. This is probably due to some internal friction in the material, not taken into account in our model.

Table 4
Belt-drive parameters.

Parameter	Symbol	Value
Radius of the pulley	R	0.027 m
Pulley central distance	L_{sp}	0.515 m
Friction coefficient	μ_0	1.2
Mass per unit length	ρ	0.096 kg/m
Mass of mounting and transducer base	m_t	20 g
Longitudinal stiffness	EA	30400 N/rib
Damping loss factor	cA	4.1 N s/rib
Bending rigidity modulus	EI	5.2×10^{-3} N m^2/rib
Rayleigh parameter	α	2.8/s
Rayleigh parameter	β	1.8×10^{-4} s

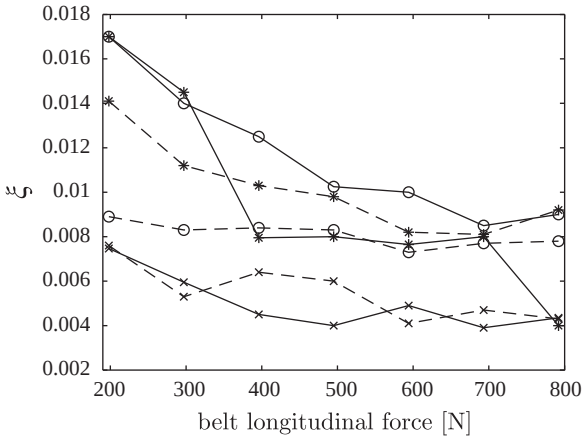

Fig. 10. Comparison between the damping ratio obtained from the measurement and from the simulation. (—×—) first mode—experiment, (- -×- -) first mode—simulation, (—○—) second mode—experiment, (- -○- -) second mode—simulation, (—∗—) third mode—experiment, (- -∗- -) third mode—simulation.

In Fig. 11 the experimentally and numerically obtained FRFs are compared at positions $L_{sp}/4$ and $L_{sp}/6$ for two different longitudinal forces. The simulated FRF is obtained using the flexible multibody model presented in Fig. 9. It can be seen that the agreement between the simulated and the experimental results is good, even at frequencies that are higher than the third natural frequency. Finally, we can conclude that the flexible, multibody, belt-drive model proposed in this study is appropriate for the modelling of belt drives, which was proven with the comparison with the experimental data.

The effect of the transducer base's mass and the mounting plate's mass is presented in Fig. 12. Simulated FRFs, obtained using the flexible, multibody belt drive are compared with the experimentally obtained FRF. It can be seen that when neglecting the mass the natural frequencies above the first mode are shifted to the left. However, the mass has practically no influence on the first natural frequency.

5. Conclusion

In this paper a belt-drive model using the ANCF is presented and a verification study was performed. The belt is modelled using beam elements and includes the damping forces. When modelling the longitudinal deformations the internal damping model is used, and in the case of bending deformations Rayleigh's proportional damping is applied. The discontinuous friction law is used for the frictional contact between the belt and the pulley. The contact is formulated as an LCP. In order to identify the damping parameters and

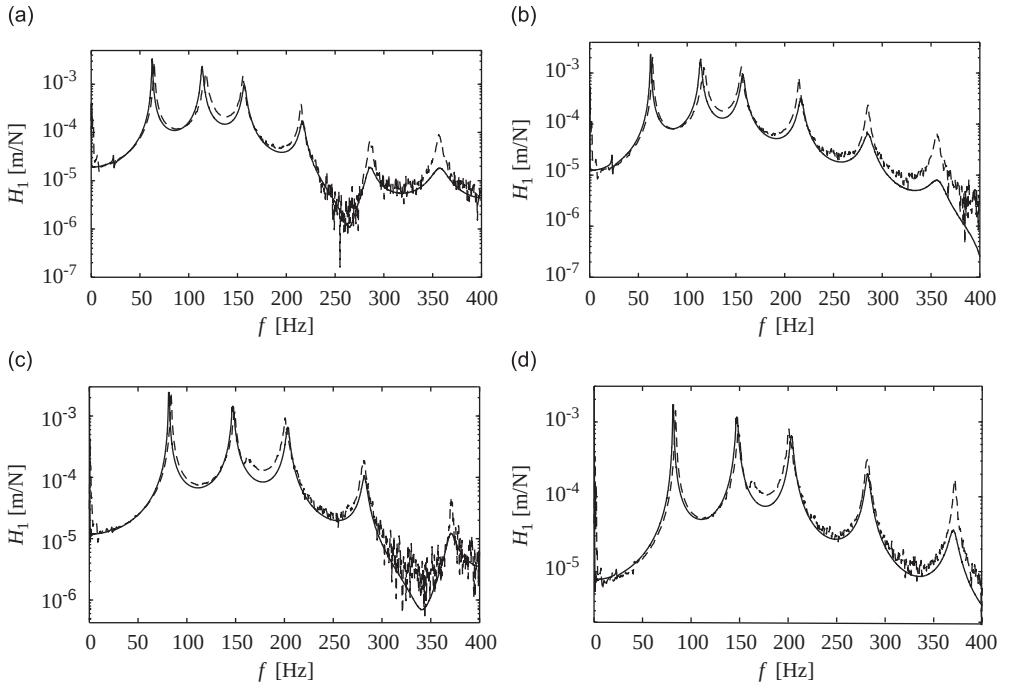

Fig. 11. Comparison between the experimentally and the numerically obtained FRFs: (a) measurement location $L_{sp}/4$, longitudinal force $F = 396\,\mathrm{N}$; (b) measurement location $L_{sp}/6$, longitudinal force $F = 396\,\mathrm{N}$; (c) measurement location $L_{sp}/4$, longitudinal force $F = 693\,\mathrm{N}$; (d) measurement location $L_{sp}/6$, longitudinal force $F = 693\,\mathrm{N}$. (- - -) experiment, (—) simulation.

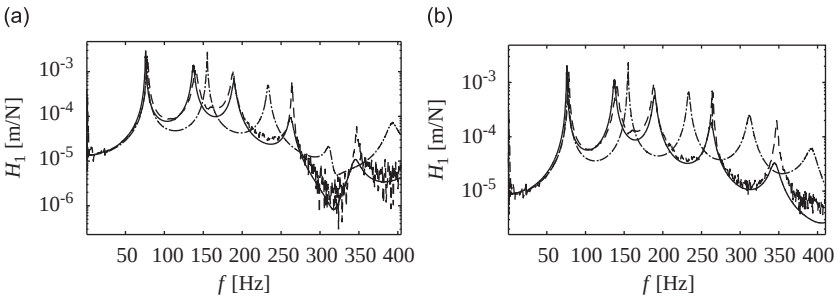

Fig. 12. Comparison between the measurement and the flexible, multibody, belt-drive model with or without additional mass: (a) measurement location $L_{sp}/4$, longitudinal force $F = 594\,\mathrm{N}$; (b) measurement location $L_{sp}/6$, longitudinal force $F = 594\,\mathrm{N}$. (- - -) experiment, (—) simulation with additional mass, (- · -) simulation without additional mass.

other material properties several experiments were conducted. The belt's longitudinal stiffness and the damping loss factor were identified from the free response of the belt-weight system. Good agreement was found between the experimentally obtained results and the simulations. The bending rigidity modulus and the Rayleigh parameters describing the damping of the bending deformations were identified using a two-pulley belt-drive system. From the free response of the belt span the bending rigidity modulus was deduced. The Rayleigh parameters were identified from the forced response of the belt span. Finally, the experimentally obtained data were incorporated into a two-pulley belt-drive numerical model and compared with the experimental data. Good agreement was obtained. We also presented the pinned–pinned beam for the modelling of the belt span and compared it with our model and the experimental data.

Although the material parameters were identified for a non-operating two-pulley belt-drive system, the presented model is general. It can be used for modelling belt drives with several pulleys and tensioner pulleys

in arbitrary operating conditions. So in future work the applicability of the presented belt-drive model should be tested when operational belt drives are considered.

Acknowledgments

This work was sponsored by the Slovenian Research Agency, under Contract 3311-04-831674, and French Rhone-Alpes Region.

References

[1] S. Abrate, Vibrations of belts and belt drives, *Mechanism and Machine Theory* 27 (1992) 645–659.
[2] S.J. Hwang, N.C. Perkins, A.G. Ulsoy, R.J. Meckstroth, Rotational response and slip prediction of serpentine belt drive systems, *Journal of Vibration and Acoustics* 116 (1994) 71–78.
[3] T.C. Kraver, G.W. Fan, J.J. Shah, Complex modal analysis of a flat belt pulley system with belt damping and coulomb-damped tensioner, *Journal of Mechanical Design* 118 (1996) 306–311.
[4] T. Iwatsubo, K. Hasegawa, S. Arii, K. Shiohata, The formulation and dynamic analysis of a multiple belt system, *Journal of Sound and Vibration* 205 (1997) 293–307.
[5] L. Manin, D. Play, P. Soleilhac, Experimental validation of a dynamic numerical model for timing belt drives behaviour simulation, in: *ASME* 2000 *Design Engineering Technical Conferences and Computers and Information in Engineering Conference*, 2000.
[6] A. Pramila, J. Laukkanen, M. Pautamo, Vibration of axially moving material using the FEM, *The American Society of Mechanical Engineers* (*Paper*) (1983) 83-DET-96.
[7] F. Pellicano, G. Catellani, A. Fregolent, Parametric instability of belts: theory and experiments, *Computers and Structures* 82 (2004) 81–91.
[8] G. Čepon, M. Boltežar, Computing the dynamic response of an axially moving continuum, *Journal of Sound and Vibration* 300 (2007) 316–329.
[9] M.J. Leamy, T.M. Wasfy, Transient and steady-state dynamic finite element modeling of belt-drives, *Journal of Dynamic Systems, Measurement, and Control* 124 (2002) 575–581.
[10] T.M. Wasfy, M.J. Leamy, Effect of bending stiffness on the dynamic and steady-state responses of belt-drives, in: *ASME* 2002 *Design Engineering Technical Conferences and Computers and Information in Engineering Conference*, 2002.
[11] A.A. Shabana, *Dynamics of Multibody Systems*, third ed., Cambridge University Press, Cambridge, 2005.
[12] K.S. Kerkkänen, D.G. Vallejo, A.M. Mikkola, Modeling of belt-drives using a large deformation finite element formulation, *Nonlinear Dynamics* 43 (2006) 239–256.
[13] K. Dufva, K.S. Kerkkänen, L.G. Maqueda, A.A. Shabana, Nonlinear dynamics of three-dimensional belt drives using the finite-element method, *Nonlinear Dynamics* 48 (2007) 449–466.
[14] G. Čepon, M. Boltežar, Dynamics of a belt-drive system using a linear complementarity problem for the belt-pulley contact description, *Journal of Sound and Vibration* 319 (2009) 1019–1035.
[15] U. Lee, H. Oh, Dynamics of an axially moving viscoelastic beam subject to axial tension, *International Journal of Solids and Structures* 42 (2005) 2381–2398.
[16] D.G. Vallejo, J. Valverde, J. Domínguez, An internal damping model for the absolute nodal coordinate formulation, *Nonlinear Dynamics* 42 (2005) 347–369.
[17] Y. Takahashi, N. Shimizu, K. Suzuki, Introduction of damping matrix into absolute nodal coordinate formulation, in: *The First Asian Conference on Multibody Dynamics*, Japan, 2002.
[18] W.S. Yoo, J.H. Lee, J.H. Sohn, S.J. Park, O. Dmitrochenko, D. Pogorelov, Comparison of physical experiments and computer simulation with ANCF: large deformation of a thin cantilever beam, in: *ASME* 2003 *Design Engineering Technical Conferences and Computers and Information in Engineering Conference*, 2003.
[19] J.H. Seo, I.H. Jung, T.W. Park, J.B. Chai, Dynamic analysis of a multibody system including a very flexible beam element, *JSME International Journal* 48 (2003) 224–233.
[20] M. Berzeri, A.A. Shabana, Development of simple models for the elastic forces in the absolute nodal co-ordinate formulation, *Journal of Sound and Vibration* 235 (2000) 539–565.
[21] F. Pfeiffer, C. Glocker, *Multibody Dynamics with Unilateral Contacts*, Wiley, New York, 1996.
[22] M.C. Ferris, T.S. Munson, Interface to PATH 3.0: design, implementation and usage, *Computational and Applied Optimization* 12 (1999) 207–227.
[23] G. Michon, L. Manin, D. Remond, R. Dufour, R.G. Parker, Parametric instability of an axially moving belt subjected to multifrequency excitations: experiments and analytical validation, *Journal of Applied Mechanics* 75 (2008) 1–8.
[24] L. Manin, F. Besson, G. Michon, R. Dufour, Experimental investigation on the dynamics characteristics of transmission belts, in: *Vibrations Chocs & Bruits*, 16*th Symposium*, Ecole Centrale Lyon, 10–12 June 2008.
[25] N.M.M. Maia, J.M.M. Silva, *Theoretical and Experimental Modal Analysis*, Wiley, New York, 1997.
[26] G. Michon, L. Manin, R.G. Parker, R. Dufour, Duffing oscillator with parametric excitation: analytical and experimental investigation on a belt–pulley system, *Journal of Computational and Nonlinear Dynamics* 3 (2008) 1–6.